ACS MATERIALS LETTERS

www.acsmaterialsletters.org

LETTER

Computational Selection of Thermally Activated Delayed Fluorescence (TADF) Molecules with Promising Electrically Pumped Lasing Property

Published as part of "Organic Functional Materials: Special Issue in Honor of Professor Daoben Zhu on His 80th Birthday".

Shiyun Lin, Qi Ou,* and Zhigang Shuai*

Cite This: *ACS Materials Lett.* 2022, 4, 487−496

Read Online

ACCESS | Metrics & More | Article Recommendations | Supporting Information

ABSTRACT: **Thermally activated delayed fluorescence (TADF) materials are competitive candidates toward electrically pumped organic lasing, because of its ability to suppress triplet accumulations by reverse intersystem crossing (RISC), especially, the multiresonance TADF (MR-TADF) compounds featuring narrow-band emission and high photoluminescence quantum yields. The goal of this work is to theoretically screen out promising electrically pumped organic laser compounds over both MR-TADF and conventional TADF molecules. We calculate the photophysical parameters over 21 organic TADF molecules to determine if the electrically pumped lasing criteria can be met, i.e., no substantial absorption/annihilation processes caused by excitons and polarons near the S_1 emission wavelength. The selection criteria include large oscillator strength of S_1, large net emission cross-section, long S_1 lifetime, and large reverse intersystem crossing rate. We are able to conclude that DABNA-2, m-Cz-BNCz, ADBNA-Me-Mes, and ADBNA-Me-Tips MR-TADF molecules are prospective candidates for electrically pumped lasing based on our theoretical protocol, and we believe this work would immediately benefit this field with better and more efficient molecular design of TADF gain materials.**

I. INTRODUCTION

In recent years, significant progress has been made in the field of organic solid-state lasers (OSSL), including the development of optical resonators integrated directly with organic semiconductors, allowing for the creation of versatile and economical OSSL devices that cover a wide range of laser wavelengths from infrared to ultraviolet.[1−5] The performance of optically pumped OSSLs has been considerably improved in the previous two decades, thanks to advances in gain media design, high-quality feedback structures, advanced encapsulation technologies, etc.[4] However, it is still challenging to realize electrically pumped lasering, because of the extremely high current density requirement expected for known materials, which mainly stems from the following factors. First, triplet excitons have a tendency to accumulate since 75% of excitons are triplets under electrical excitation based on spin statistics.[6] The long-lived triplet excitons cause the light amplification to be quenched through triplet−triplet absorption (TTA) and S_1 population reduced via singlet−triplet annihilation (STA) governed through the overlap of the broad TTA band and the fluorescence emission band.[3] In fact, experimental works have suggested that STA and TTA are the most important contributors in optical losses in the electrically pumped devices.[7,8] In addition, polarons, excitons, and other species will cause further annihilation and absorption losses under current injection, which are not involved in optical pumping lasers.[3] Because of these unfavorable losses, electrically pumped OSSLs are yet to be maturely developed.

One alternate approach to eliminate the accumulation of triplet excitons is to use the triplet gain media including

Received: December 15, 2021
Accepted: February 4, 2022

Downloaded via TSINGHUA UNIV on February 23, 2022 at 06:25:34 (UTC).
See https://pubs.acs.org/sharingguidelines for options on how to legitimately share published articles.

© XXXX American Chemical Society

https://doi.org/10.1021/acsmaterialslett.1c00794
ACS Materials Lett. 2022, 4, 487−496

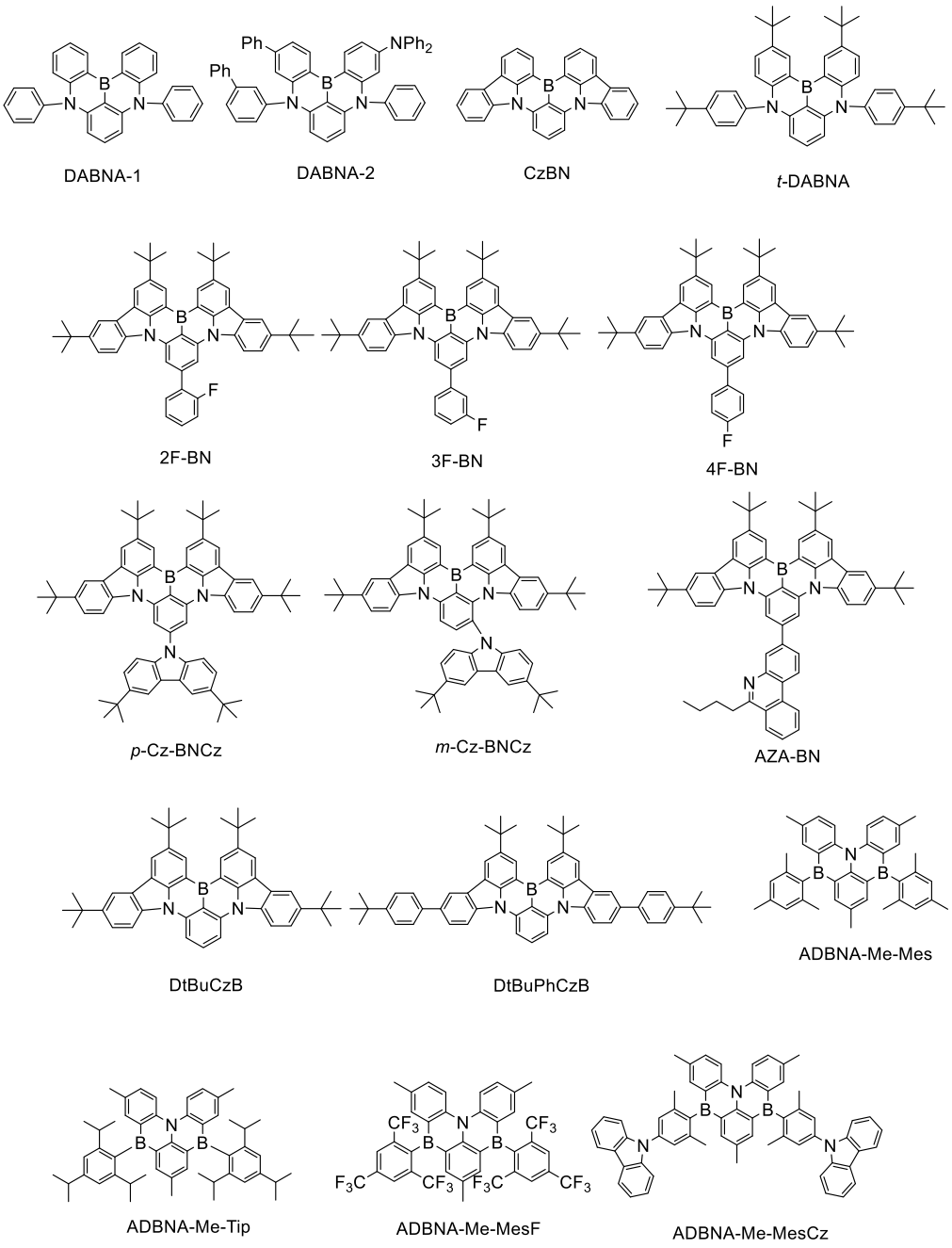

Figure 1. Group I: MR-TADF molecules investigated in this work. Most of the MR-TADF molecules are selected from ref 23, as well as a few recently published molecules.

thermally activated delayed fluorescence (TADF) and phosphorescence emitters.[9] In principle, all of the triplet excitons formed under current injection could be harvested via reverse intersystem crossing (RISC) and utilized for electroluminescence in TADF materials, which would be highly beneficial to the reduction of the injected current density required by electrically pumped OSSLs.[4,10] However, the oscillator strength of S_1 is severely suppressed in conventional TADF molecules, because of the CT character of S_1-to-S_0 transition,[11−15] giving rise to an extremely small emission cross section that is detrimental to light amplification. Although a few conventional TADF compounds have been investigated as laser gain media under optical pumping by multiple groups,[16−21] the required pumping thresholds of these materials are significantly higher than the lowest reported values of prompt fluorescence materials. Therefore, the realization of light amplification on conventional TADF materials is still cumbersome, let alone the electrically pumped lasing.

To circumvent the shortcomings of conventional TADF materials, a landmark design strategy called "multiresonance thermally activated delayed fluorescence" (MR-TADF) was proposed by Hatakeyama and co-workers.[22] In 2016, a stiff polycyclic aromatic framework containing electron-deficient and electron-rich atoms was discovered, offering a pair of effectively separated frontier orbitals via multiple resonance effects. Compared with conventional TADF molecules, MR-TADF compounds acquire significantly enhanced oscillator

https://doi.org/10.1021/acsmaterialslett.1c00794
ACS Materials Lett. 2022, 4, 487−496

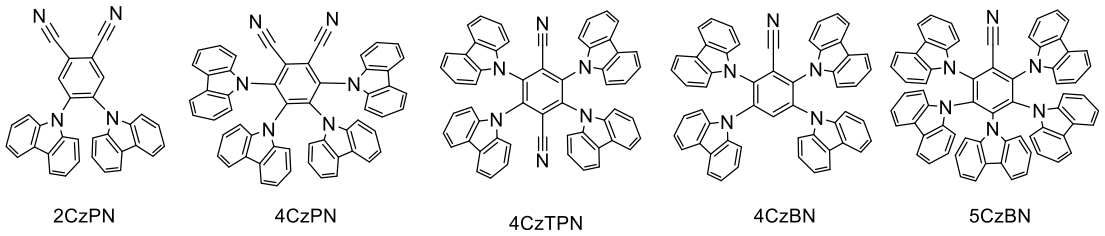

Figure 2. Group II: Conventional TADF molecules investigated in this work. These TADF molecules are chosen from ref 29.

strength, thanks to their rigid framework, which is preferred in light amplification.[23] Nevertheless, while lasing behaviors under optical pumping via MR-TADF materials have been reported,[24] the drawbacks of MR-TADF compounds have also been noticed, including their relatively slow RISC rate and the small Stokes shift that would lead to unfavorable self-absorption.[24] Until now, a comprehensive evaluation of the ability to realize lasing (especially electrically pumped lasing) among massive existing TADF materials is yet to be made.

Bearing these in mind, the goal of this work is to select prospective candidates for electrically pumped lasing over a wide range of organic TADF molecules following the computational screen-out protocol previously reported by our group.[25] The capacity to realize generic laser will be assessed over a series of MR-TADF molecules and a few conventional TADF molecules (shown in Figures 1 and 2, respectively) via density functional theory (DFT), time-dependent density functional theory (TDDFT), and high-level correlated wave function calculations under these criteria: no significant absorption or annihilation among excitons and polarons around the fluorescence emission wavelength, efficient RISC process for triplet harvesting, and relative long delayed fluorescence lifetime were observed. With the formerly mentioned criteria and the photophysical properties calculated by our self-developed molecular material property prediction software package (MOMAP),[26−28] we are able to select four promising MR-TADF candidates in realizing electrical pumping laser, i.e., DABNA-2, m-Cz-BNCz, ADBNA-Me-Mes, and ADBNA-Me-Tips, and the computational protocol we present here can be applied to upcoming novel TADF materials, so that more promising candidates can be efficiently explored.

II. RESULTS AND DISCUSSION

II.1. Investigated Molecule Systems and Predicted Emission Energies. Investigated TADF molecules in this work are mainly selected from experimental works from ref 23 for group I and ref 29 for group II, as well as a few recently published molecules. The photoluminescence (PL) properties of these selected molecules have been experimentally demonstrated, and lasing behaviors of DABNA and 4CzTPN have been reported,[19,24] providing a reliable benchmark for our computational results.

TD-B3LYP/6-31G(d) for group I and TD-wb97xd/6-31G//TD-CAM-B3LYP/6-31G(d) for group II (TD-CAM-B3LYP/6-31G(d) refers to the excited-state geometry optimized with CAM-B3LYP model and 6-31G(d) basis, whereas TD-wb97xd/6-31G(d) refers to excited-state energies obtained with wb97xd functional and 6-31G(d) basis). We compare the predicted emission energies with experimental values for all the investigated systems in Table S1 in the electronic Supporting Information (ESI). It can be seen that, for these materials, the absolute error anticipated by theoretical predictions is consistently minor. The largest deviation for group I is 0.282 eV, from AZA-BN, while the largest deviation for group II is −0.199 eV, from 5CzBN, both of which are within the TDDFT method's reliable deviation range (∼0.3 eV). Furthermore, the mean absolute error (MAE) for group I is 0.132 eV, while the MAE for group II is even smaller. Overall, these precise predictions indicate the rationality of TD-B3LYP/6-31G(d) for group I and TD-wb97xd/6-31G//TD-CAM-B3LYP/6-31G(d) for group II in calculating the excitation energies of the TADF molecules investigated throughout this work.

Note that even though TD-B3LYP/6-31G(d) for group I provides reasonable emission energies for the investigated compounds, it fails to provide accurate predictions on the singlet−triplet energy gap for MR-TADF systems, with a consistent overestimation of ∼0.250 eV (see Table S4 in the ESI). Similar overestimation of ΔE_{ST} has been reported in the work by Olivier et al.,[30] who suggest tackling the singlet−triplet energy gap with second-order approximate coupled cluster (SCS-CC2) method for MR-TADF materials. Therefore, we apply SCS-CC2 to evaluate ΔE_{ST} for MR-TADF compounds (while keeping the TD-B3LYP/6-31G(d) for group I excitation energies, because of the overestimation of SCS-CC2 of excitation energies, as shown in Table S5 in the ESI). The resulting MAE of ΔE_{ST} is ∼0.031 eV for the investigated MR-TADF materials (see Table S2 in the ESI). It is worthwhile to mention that accurate predictions on ΔE_{ST} have also been recently proposed within the combination of unrestricted Kohn−Sham and restricted open-shell Kohn−Sham framework,[31] as well as with the optimally tuned range-separated hybrid functional.[32] For group II, the TD-wb97xd/6-31G//TD-CAM-B3LYP/6-31G(d) is able to properly describe ΔE_{ST}, with an MAE of ∼0.111 eV.

II.2. Emission Oscillator Strength and Light Amplification. For laser gain medium, the stimulated emission cross section σ_{em} of a laser transition is a critical parameter that can affect laser performance, in terms of output energy, threshold energy, maximum gain, etc. A large σ_{em} is required for a good laser gain medium in conventional lasing mechanisms. Theoretically, σ_{em} is directly proportionate to the emission oscillator strength f_{em} via[33]

$$\sigma_{em}(\upsilon) = \frac{e^2}{4\varepsilon_0 m_e c_0 n_F} g(\upsilon) f_{em} \quad (1)$$

where e the electron charge, ε_0 the vacuum permittivity, m_e the mass of electron, c_0 the speed of light, n_F the refractive index of the gain material, υ the frequency of the corresponding emission, and $g(\upsilon)$ the normalized line shape function with $\int g(\upsilon)\, d\upsilon = 1$. We compute f_{em} from electronic structure calculations, and plot f_{em} for all investigated materials in Figure 3. For molecules in group I, ADBNA-Me-MesCz has a

https://doi.org/10.1021/acsmaterialslett.1c00794
ACS Materials Lett. 2022, 4, 487−496

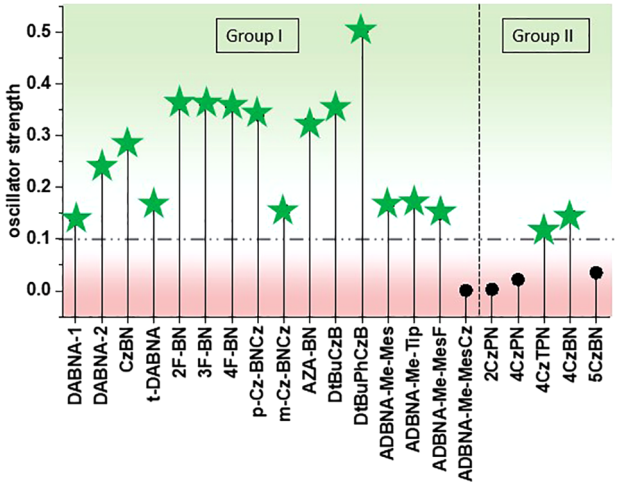

Figure 3. Emission oscillator strength f_{em} of all the investigated materials. Oscillator strengths for the investigated systems in group II are evaluated with the HT effect taken into account. The red area indicates smaller oscillator strengths that are not favored in realizing light amplification, while the green area is preferred oscillator strengths.

significantly smaller f_{em} ($\leq$0.1) compared to other molecules. For molecules in group II, the zeroth-order transition dipoles are hindered, because of their highly symmetric structure, i.e., these molecules possess a symmetry forbidden S_1.[34] Consequently, it is necessary to take the Herzberg–Teller (HT) effect into consideration and evaluate the vibrational-induced oscillator strengths[35] (see Table S7 in the ESI for explicit numbers). As seen in Figure 3, in this part, ADBNA-Me-MesCz, 2CzPN, 4CzPN, and 5CzBN are excluded from the candidates of electrical pumping organic laser materials, because of their exceptionally small oscillator strengths.

II.3. Computational Selection of Electrically Pumped Lasing Candidates. To achieve electrical pumping lasers, the unfavorable losses introduced via the following factors must be avoided. First, the $S_0 \rightarrow S_1$ self-absorption, as well as photoinduced absorptions around the S_1 emission wavelength by excitons and polarons to higher excited states ($S_1 \rightarrow S_n$, $T_1 \rightarrow T_n$, $D_0^+ \rightarrow D_n^+$, $D_0^- \rightarrow D_n^-$, where $D^{\pm}$ refers to polarons) will reduce the effective stimulated emission cross section of S_1. Second, fluorescence resonance energy transfer processes can cause singlet excitons to annihilate with singlet/triplet excitons and polarons. Third, the accumulation of the triplet excitons will aggregate triplet losses, presumably leading to the degradation of the lasing material.[3] *Note that, unlike prompt fluorescent laser materials, the ISC from S_1-to-triplet states in TADF materials is not a detrimental factor, because the resulting triplet excitons are expected to upconvert to S_1 via efficient RISC process.* A fast RISC rate constant is thus favored, which potentially prevents the accumulation of triplets and boosts the population of the lasing (S_1) state.

We begin with an estimation of the stimulated emission cross section of S_1 using eq 1. We rewrite σ_{em} as a function of wavelength for convenience by inserting $g(\upsilon) = \frac{g(\lambda)\,d\lambda}{d\upsilon} = g(\lambda)\frac{\lambda^2}{c_0}$ into eq 1:[33]

$$\sigma_{em}(\lambda) = \frac{e^2\lambda^2}{4\varepsilon_0 m_e {c_0}^2 n_F} g(\lambda) f_{em} \tag{2}$$

where $g(\lambda)$ is the normalized line shape function expressed in the emission wavelength domain, using the equation $\int g(\lambda)\,d\lambda = 1$. We apply a universal Gaussian broadening to group II according to their experimental spectra with a 100 nm full-width at half-maximum (FWHM).[19] For group I, because of their narrow-band emission with 2–3 vibration peaks (as shown in Figure S1 in the ESI), a 30 nm FWHM for each vibration peak is set for each molecule, except for ADBNA derivatives, for which a 45 nm FWHM is set, because of the veiled vibration peaks that are not clearly exhibited (see Figure S1). The refractive index is set to be 1.5, which follows the parameter set for thin film materials in ref 25. Note that the oscillator strengths of the vibration peaks for group I are

Table 1. Values of S_1 Emission Cross Section and Varied Absorption Cross Sections at the 0-0 or 0-1 Transition Wavelength of 17 Candidates[a]

molecule	σ_{em}	$\sigma_{abs}^{S_0\rightarrow S_1}$	$\sigma_{abs}^{S_1\rightarrow S_n}$	$\sigma_{abs}^{T_1\rightarrow T_n}$	$\sigma_{abs}^{D_0+\rightarrow D_n^+}$	$\sigma_{abs}^{D_0-\rightarrow D_n^-}$	$\sigma_{eff}^{net,opt}$	$\sigma_{eff}^{net,ele}$
DABNA-1[c]	0.297	0.000	0.000	0.000	0.002	1.006	0.297	N/A[b]
DABNA-2[c]	2.825	0.008	0.623	0.599	0.058	0.280	2.194	1.258
CzBN[c]	1.612	0.096	0.540	0.411	0.224	0.000	0.976	0.341
t-DABNA[c]	1.328	0.052	1.800	0.689	0.000	0.131	N/A[b]	N/A[b]
2F-BN[c]	1.475	0.036	0.736	0.749	0.377	1.491	0.704	N/A[b]
3F-BN	10.287	8.410	0.539	2.755	0.027	0.208	1.337	N/A[b]
4F-BN[c]	1.448	0.046	0.010	0.104	0.326	1.198	1.393	N/A[b]
p-Cz-BNCz[c]	0.951	0.008	0.736	1.000	0.115	0.580	0.207	N/A[b]
m-Cz-BNCz	4.821	3.346	0.015	0.000	0.042	0.203	1.460	1.215
AZA-BN[c]	1.612	0.096	0.540	0.411	0.224	0.000	0.976	0.341
DtBuCzB[c]	1.644	0.059	0.001	1.082	0.000	0.000	1.584	0.501
DtBuPhCzB[c]	2.576	0.108	0.102	0.008	0.000	0.000	2.366	2.358
ADBNA-Me-Mes	3.375	0.164	0.369	0.278	0.412	0.039	2.842	2.114
ADBNA-Me-Tip	3.494	0.268	0.162	0.059	0.290	0.067	3.064	2.648
ADBNA-Me-MesF	3.230	0.054	0.172	0.269	0.000	0.007	3.005	2.728
4CzTPN	1.048	0.404	0.120	0.442	0.464	0.005	0.523	N/A[b]
4CzBN	1.191	0.346	0.225	0.305	0.463	0.212	0.620	N/A[b]

[a]Values are displayed in units of 10^{-17} cm^2. [b]The effective stimulated emission cross section is anticipated to be negative. [c]Values of S_1 emission cross section and varied absorption cross sections are at 0–1 emission peak, and the values of various cross sections at 0–0 emission peaks are shown in Table S8 in the Supporting Information.

https://doi.org/10.1021/acsmaterialslett.1c00794
ACS Materials Lett. 2022, 4, 487–496

Table 2. Theoretical Photophysical Parameters of 17 Candidates

molecule	k_r^S (s^{-1})	k_{nr}^S (s^{-1})	k_{ISC} (s^{-1})	k_{RISC} (s^{-1})	k_{nr}^T (s^{-1})	τ_{PF} (ns)	τ_{DF} (μs)	τ_{S1} (ns)
DABNA-1	4.40×10^7	1.11×10^7	9.15×10^5	5.96×10^3	6.19×10^3	17.9	83.0	18.0
DABNA-2	7.02×10^7	1.10×10^7	9.19×10^5	1.14×10^4	9.16×10^3	12.2	48.9	12.3
CzBN	8.32×10^7	1.38×10^7	1.10×10^5	1.82×10^4	5.11×10^3	10.3	43.0	10.3
t-DABNA	5.24×10^7	1.19×10^7	1.31×10^6	8.74×10^3	1.29×10^3	15.2	102	15.5
2F-BN	9.92×10^7	1.64×10^7	1.48×10^4	4.49×10^3	8.80×10^3	8.65	75.3	8.65
3F-BN	9.91×10^7	1.66×10^7	1.10×10^4	2.60×10^3	9.16×10^3	8.64	85.0	8.64
4F-BN	1.00×10^8	1.60×10^7	3.27×10^4	8.09×10^3	9.71×10^3	8.62	56.2	8.62
p-Cz-BNCz	9.86×10^7	1.50×10^7	2.06×10^5	3.84×10^4	6.34×10^3	8.78	22.4	8.80
***m*-Cz-BNCz**	3.52×10^7	1.32×10^7	4.56×10^6	4.10×10^5	7.87×10^3	18.9	2.6	20.6
AZA-BN	8.54×10^7	1.65×10^7	1.28×10^4	4.37×10^3	7.35×10^3	9.81	85.3	9.81
DtBuCzB	1.01×10^8	1.49×10^7	1.03×10^5	1.97×10^4	5.71×10^1	8.64	50.6	8.65
DtBuPhCzB	1.36×10^8	1.47×10^7	3.33×10^5	6.64×10^3	7.79×10^3	6.62	69.4	6.63
ADBNA-Me-Mes	4.55×10^7	1.46×10^7	7.73×10^6	8.34×10^4	3.12×10^4	14.7	9.51	16.1
ADBNA-Me-Tip	4.30×10^7	1.60×10^7	2.29×10^6	3.33×10^4	3.10×10^4	16.3	15.9	16.6
ADBNA-Me-MesF	3.60×10^7	1.59×10^7	1.36×10^6	1.20×10^4	3.04×10^4	18.8	23.8	18.9
4CzTPN	2.51×10^7	1.35×10^7	3.12×10^8	5.96×10^6	5.16×10^{-3}	2.85	1.53	25.6
4CzBN	4.68×10^7	9.78×10^6	3.54×10^8	7.61×10^4	2.06×10^4	2.43	32.2	7.57

redistributed by the emission spectrum calculated by MOMAP (see Table S6 in the ESI). The absorption cross section between S_1/S_n, T_1/T_n, D_0^+/D_n^+, and D_0^-/D_n^- can give rise to strong absorption in the vicinity of S_1 emission wavelength. The absorption cross section is determined in the same way as the emission cross section via

$$\sigma_{abs}^{X_i \to X_j}(\lambda) = \frac{e^2\lambda^2}{4\varepsilon_0 m_e c_0^2 n_F} g(\lambda) f_{abs}^{X_i \to X_j} \quad (3)$$

where $f_{abs}^{X_i \to X_j}$ denotes the oscillator strengths of various absorption ($X_i \to X_j$=$S_1 \to S_n$, $T_1 \to T_n$, $D_0^+ \to D_n^+$ and $D_0^- \to D_n^-$). For each molecule, same Gaussian broadening is set for $\sigma_{abs}^{X_i \to X_j}(\lambda)$ as the one applied in $\sigma_{em}(\lambda)$. Finally, we compute all rate constants involved in the TADF process via thermal vibration correlation function (TVCF) rate formalism, and calculate the decay lifetime of emission for the remaining 17 candidates to qualitatively assess the optical pumping threshold power. Explicit numbers of estimated σ_{em} and $\sigma_{abs}^{X_i \to X_j}$ for these 17 molecules are listed in Table 1, while the rate constants of the main photophysical process are given in Table 2 (radiation of T_1 is ignored because of its considerably longer time scales). Note that MR-TADF molecules (group I) may exhibit lasing/ASE behavior at either 0−0 or 0−1 transition wavelength, which is dependent on the values of net emission cross section, and the one with larger $\sigma_{eff}^{net,opt}$ is listed in Table 1 while the other one is listed in Table S8 in the ESI.

The theoretical predicted photoluminescence quantum yield (PLQY) is compared to experimental data (see Table S8), and the theoretical values are in good agreement with the experimental results. (Computational details of PLQY can be found in the ESI.)

We first examine the optical pumping laser performance of these screened-out systems, where polaron-induced losses play no role. Under optical pumping, the net stimulated emission cross section is defined as[25]

$$\sigma_{eff}^{net,opt} = \sigma_{em} - \sigma_{abs}^{S_0 \to S_1} - \sigma_{abs}^{S_1 \to S_n} \quad (4)$$

According to eq 4, we calculate the value of $\sigma_{eff}^{net,opt}$ at S_1 emission wavelength for 17 candidates, as shown in Table 1. Sixteen candidates possess a positive net stimulated emission cross section, and ADBNA-Me-Tips shows the largest value at 3.064×10^{-17} cm^2 over the 16 candidates, which is close to the magnitude of the conventional laser materials of $\sim 0.7-1.5 \times 10^{-16}$ cm^2, as reported in ref 36.

The threshold power (P^{th}) is inversely proportional to the product of the lifetime of S_1 and the effective stimulated emission cross section at the lasing wavelength under the condition of optical pumping.[37] Population inversion is favored by longer S_1 lifetime, which is a need for traditional lasing mechanism and is again validated in ref 25. Among MR-TADF systems, m-Cz-BNCz and ADBNA derivatives shows longer average lifetime of S_1 for the sake of more effective ISC and RISC processes than other molecules in group I, as shown in Table 2 (computational details of lifetime can be found in the ESI). To qualitatively evaluate the threshold power of these 16 candidates, we plot the value of $1/\sigma_{eff}^{net,opt}\tau_{S_1}$ in Figure 4 and find that eight candidates have values smaller than $1/\sigma_{eff}^{net,opt}\tau_{S_1}$ that lie in the green area, indicating a possibly lower threshold

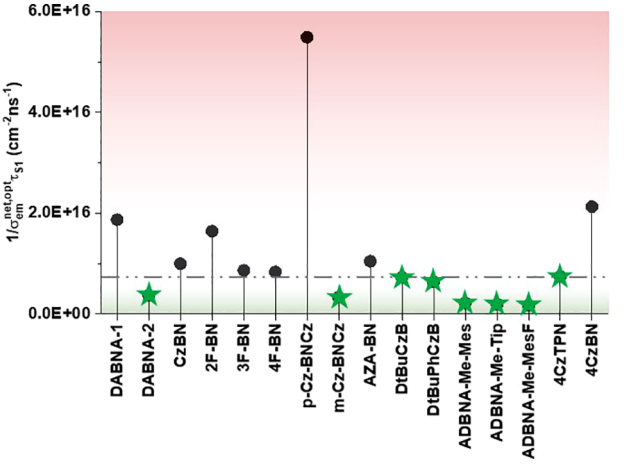

Figure 4. Calculated $1/[\sigma_{em}^{net,opt} \times \tau_{S1}]$ of 16 candidates. The threshold power P^{th} is inversely proportional to $1/[\sigma_{em}^{net,opt} \times \tau_{S1}]$, and, therefore, larger $1/[\sigma_{em}^{net,opt} \times \tau_{S1}]$ (red area) indicates a presumably higher threshold power, which is unfavored in realizing light amplification. Contrarily, smaller $1/[\sigma_{em}^{net,opt} \times \tau_{S1}]$ (green area) is preferred.

https://doi.org/10.1021/acsmaterialslett.1c00794
ACS Materials Lett. 2022, 4, 487−496

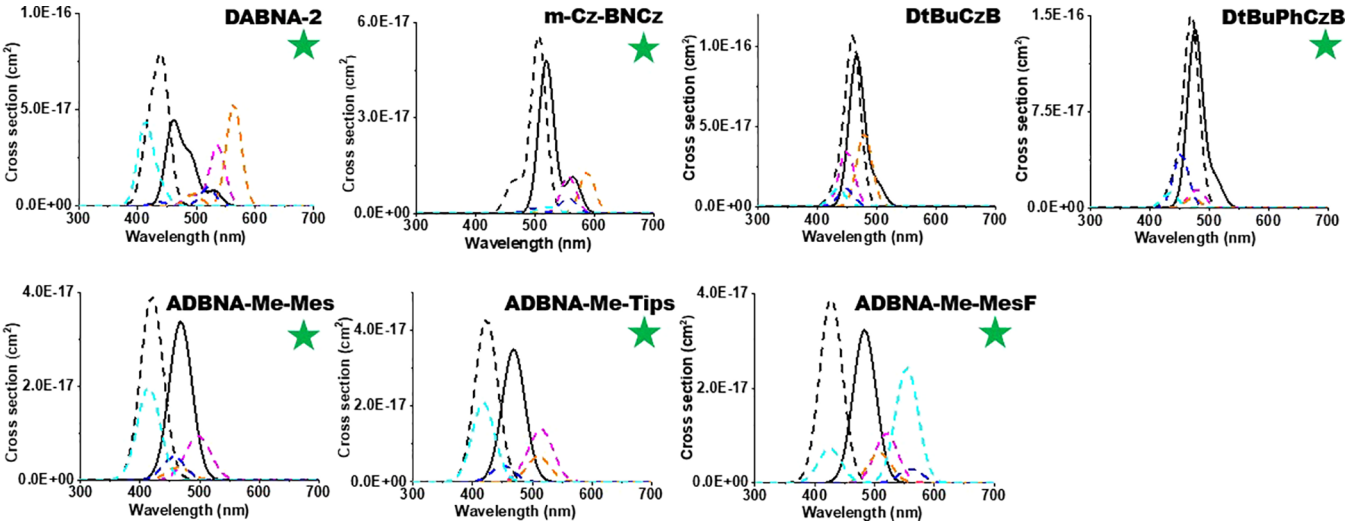

Figure 5. Theoretically simulated S_1 emission cross sections and varied absorption cross sections. Black solid line and black dashed line correspond to the stimulated emission cross section and self-absorption cross section of S_1, respectively. Varied absorption cross sections introduced by $S_1 \rightarrow S_n$ (magenta dashed), $T_1 \rightarrow T_n$ (orange dashed), $D_0^+ \rightarrow D_n^+$ (blue dashed) and $D_0^- \rightarrow D_n^-$ (cyan dashed) are plotted around the emission wavelength ($\pm$125 nm).

power. Among these eight candidates, 4CzTPN has the largest $1/\sigma_{\text{eff}}^{\text{net,opt}}\tau_{S_1}$. As experimentally reported in ref 9, the threshold power for 4CzTPN is 1.96×10^5 kW cm^{-2}. Therefore, we expect that the threshold power of optically pumped lasing of the remaining seven candidates is lower than that of 4CzTPN.

Moving to the electrical pumping scenario, we evaluate the net emission cross section that is intuitively defined in ref 25 via

$$\sigma_{\text{eff}}^{\text{net,ele}} = \sigma_{\text{em}} - \sigma_{\text{abs}}^{S_0 \rightarrow S_1} - \sigma_{\text{abs}}^{S_1 \rightarrow S_n} - n\sigma_{\text{abs}}^{T_1 \rightarrow T_n} - \sigma_{\text{abs}}^{D_0^+ \rightarrow D_n^+} - \sigma_{\text{abs}}^{D_0^- \rightarrow D_n^-} \quad (5)$$

Table 1 lists the explicit numbers of $\sigma_{\text{eff}}^{\text{net,ele}}$, while Tables S6 and S7 in the ESI list explicit transition energies and corresponding oscillator strengths. From Table 1, both of the remaining conventional TADF candidates, 4CzTPN and 4CzBN suffer from the drastic losses induced by singlet exciton and/or triplet exciton and possess negative $\sigma_{\text{eff}}^{\text{net,ele}}$ values. As a result, even though the RISC-boosted optical lasing behavior is observed experimentally for 4CzTPN,[19] these conventional TADF compounds are not expected to be prospective candidates for the electrical pumping laser.

In Figure 5, we plot the stimulated emission cross section of S_1 and varied absorption cross sections around the S_1 emission wavelength ($\pm$125 nm, with the corresponding energy range $\pm$0.5−1 eV) for the seven remaining MR-TADF candidates, which present positive net emission cross section under electrical pumping at either 0−0 or 0−1 transition wavelength. According to Figure 5 and Table 1, DtBuCzB and DtBuPhCzB severely suffer from $S_0 \rightarrow S_1$ self-absorption. Hence, the light emission of these molecules can be more effectively amplified at the 0−1 transition wavelength instead of the 0−0 transition peak, which is consistent with the experimental results.[24] In contrast, for the remaining candidates, the 0−0 transition peaks are more likely to be amplified, compared to the 0−1 transition due to the subtle self-absorption from $S_0 \rightarrow S_1$. It can be seen from Figure 5 that most of the candidates in group I are not extensively affected by the singlet exciton-induced losses, and therefore they satisfy the condition of the optical pumping laser. Six candidates—DABNA-2, m-Cz-BNCz, DtBuPhCzB, ADBNA-Me-Mes, ADBNA-Me-Tips, and ADBNA-Me-MeF—possess larger net emission cross sections ($\sigma_{\text{eff}}^{\text{net,ele}} \geq 1.2 \times 10^{-17}$ cm^2). DtBuPhCzB and ADBNA-Me-MeF are further excluded, because these two molecules have larger k_{nr}^{T} than k_{RISC}, which makes the RISC boosting singlet harvesting less efficient. Altogether, we conclude that DABNA-2, m-Cz-BNCz, ADBNA-Me-Mes, and ADBNA-Me-Tips have the greatest electrically pumped laser among these selected systems.

II.4. Toward the Design of MR-TADF Materials with High Laser Performance. The four lasing candidates that have been screened out in the last section can be divided into two categories: one has a small Stokes shift and the shoulder vibrational emission peak is amplified (such as DABNA-2), and the other has a larger Stokes shift and the main emission peak is amplified (such as m-Cz-BNCz and ADBNA derivatives). The self-absorption loss is alleviated either via the amplification of the shoulder peak or the relatively large Stokes shift.

For DABNA-2, the strength of the 0−1 vibrational emission peak is much more significant than other MR-TADF molecules, as shown in Figure S1, which turned out to be the peak with the larger net emission cross section, compared to the main peak, of which the net emission cross section is severely deduced by the self-absorption, as shown in Figure 5 and Table S10 in the ESI. In Figure 6, the individual emission peaks are assigned to specific vibrational modes for DABNA-2 via the sum-overstates method. The 0−1 vibrational peaks are basically derived from the modes with medium frequencies (975.84, 1016.67, and 1058.96 cm^{-1}) and relatively large Huang−Rhys factors (>0.15). These vibrational modes correspond to the deformation and vibration of branched benzene rings. Therefore, for MR-TADF molecules with a small Stokes shift, the involvement of branched benzene rings is essential to induce sufficiently strong vibrational peaks that potentially possess a large net emission cross section.

Among the investigated MR-TADF molecules, the ADBNA derivates and m-Cz-BNCz present larger Stokes shifts than other molecules (see Figure S1, as well as Figure 5). As shown in Figure 7a, we use the sum-over-state method to calculate the

https://doi.org/10.1021/acsmaterialslett.1c00794
ACS Materials Lett. 2022, 4, 487−496

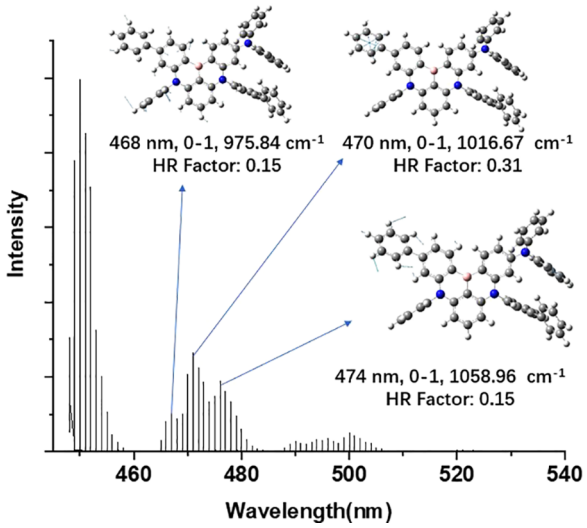

Figure 6. Theoretically calculated vibrationally resolved emission spectra at 0 K of DABNA-2. The individual emission peaks can be allocated to the related vibrational modes, which are labeled on the picture.

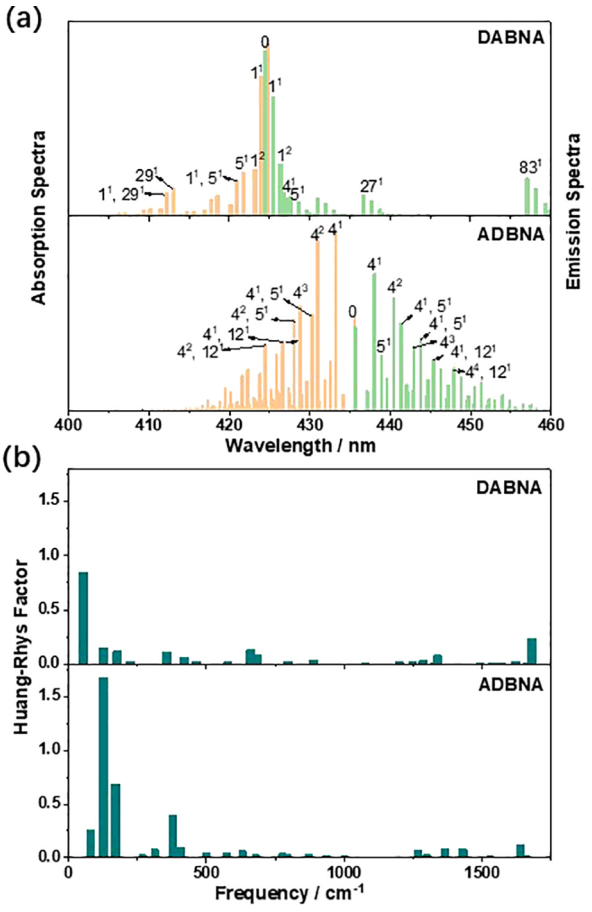

Figure 7. (a) Absorption and emission spectra at 0 K of DABNA and ADBNA, and the assignments of typical peaks with n^m, where n is the normal mode index and m the vibrational quantum number; (b) Huang−Rhys Factor of DABNA and ADBNA versus normal-mode frequency at the S_0 potential energy surface.

absorption and emission spectra of DABNA and ADBNA at 0 K, as well as the assignments of typical peaks, in order to gain insight into such diverse spectral behaviors of ADBNA and DABNA derivatives. Different from DABNA, the maximum peak of ADBNA appears at the 0−1 transition, which mainly stems from the fact that low-frequency vibration modes with a large Huang−Rhys factor in ADBNA induce rather strong 0−1 and 0−2 vibrational peaks, as shown in Figure 7b, leading to a suppressed 0−0 transition peak and a larger Stokes shift, compared to DABNA.

Figure S2 in the ESI shows the reorganization energy projection of m-Cz-BNCz and p-Cz-BNCz to further analyze the role of the carbazole functional group. The enlarged reorganization energy of m-Cz-BNCz can be attributed to the dihedral angle torsion between the carbazole group and BNCz moiety (see Figure S2), whereas it is insignificant for p-Cz-BNCz.

Consequently, to design the TADF laser material with a relatively larger Stokes shift, to alleviate the self-absorption loss to the main peak, one could (i) apply the ADBNA as a body structure, because of the vibrational peaks induced by the low-frequency vibrational modes, and (ii) construct meta-substituted compounds that possess extra flexibility than the para-substituted one.

III. CONCLUSION

In conclusion, by employing well-benchmarked electronic structure approaches, DFT/TDDFT and SCS-CC2, and TVCF rate formalism, as implemented in home-built program MOMAP for radiative and nonradiative interstate conversion rates and excited-state lifetimes, we have investigated plausible lasing behaviors among a series of organic TADF materials, followed by a systematic computational selection of electrically pumped lasing candidates, according to the criterion that prospective candidates must have a large net stimulated emission cross section that avoids severe absorption/annihilation processes caused by singlet and triplet excitons and/or polarons around the S_1 emission wavelength, which are verified via the absorption cross sections of $S_0 \rightarrow S_1$, $S_1 \rightarrow S_n$, $T_1 \rightarrow T_n$, $D_0^+ \rightarrow D_n^+$ and $D_0^- \rightarrow D_n^-$, and an efficient RISC process that can suppress the accumulations of triplets. Based on the criteria and the photophysical parameters obtained by MOMAP, four prospective candidates (i.e., DABNA-2, m-Cz-BNCz, ADBNA-Me-Mes, and ADBNA-Me-Tips) have been predicted of a great promise in achieving electrically pumped lasing. All four of these materials are MR-TADF molecules and possess relatively slower nonradiative decay rate of T_1 than their RISC rate. No significant absorption cross section of any species has been detected, in comparison to the large stimulated emission cross section of these four molecules. Based on spectrum assignment and reorganization energy analysis of the screened-out promising TADF laser materials, two substantial molecular design principles toward MR-TADF materials with high laser performance are proposed: (i) molecules with a small Stokes shift require branched substitutes to induce sufficiently strong vibrational peaks to be amplified; and (ii) the body structure of ADBNA with strong low-frequency vibrational peaks and reorganization energy increased via meta-substitution to induce larger Stokes shift to avoid self-absorption. While the development of TADF-based laser is vigorous and ongoing, we believe the protocol and theoretical findings proposed in this work would immediately benefit this field by providing better and more efficient molecular design of TADF gain materials.

https://doi.org/10.1021/acsmaterialslett.1c00794
ACS Materials Lett. 2022, 4, 487−496

IV. METHODS

IV.1. Electronic Structure Calculations. Unless otherwise noted, all computations in this work use the 6-31G(d) basis set. The geometries of singlet ground states are optimized by a normal restricted DFT calculation, while geometry and excitation energy of singlet excited states are generated via restricted TDDFT. The triplet states are optimized using an unrestricted DFT method. What's more, the dispersion-correction D3 is performed throughout the DFT calculations. For MR-TADF molecules, the B3LYP functional is applied to geometrical optimizations and frequency calculations. The excitation energy is obtained from DFT calculations, while the ΔE_{ST} value is calculated by a high-level wave function SCS-CC2 method with the def2-TZVP basis set for a more-accurate description, and the excitation energy of T_1 is corrected after that. For the conventional TADF molecules, since the B3LYP functional cannot give a reliable prediction to CT excited states.[38,39] A reliable method is verified for conventional TADF molecules by Brédas et al.[40] Therefore, an optimal-tuning ωb97xd functional is used to obtain the electronic structures and frequencies of optimized ground states and excited states in Tamm−Dancoff approximation (TDA). The geometrical optimization of the ground state is taken from B3LYP method, while that for CAM-B3LYP is obtained for excited states. All of the quantum chemistry calculations are performed in Gaussian 16,[41] except for the SCS-CC2 calculations in TURBOMOLE 7.4.[42] The nonadiabatic coupling and spin−orbit coupling are evaluated at the same level at S_1 and T_1 optimized geometry, respectively, in the Q-Chem 5.3 program.[43]

IV.2. Photophysical Property Calculations. The radiative decay rate constant can be calculated by an integration across the emission spectrum: $k_r(T) = \int \sigma_{em}(\omega,T)\, d\omega$, where $\sigma_{em}(\omega,T)$ can be calculated using the Fermi Golden Rule (FGR):

$$\sigma_{em}(\omega, T) = \frac{2\omega^3}{3\pi\hbar c^3} |\boldsymbol{\mu}_{fi}|^2 \int_{-\infty}^{+\infty} e^{-i(\omega-\omega_{if})t} \rho_{em}(t, T)\, dt \tag{6}$$

Here, μ_{fi} is the transition dipole moment between the initial and final electronic states, and $\rho_{em}(t, T) = Z_i^{-1}\mathrm{Tr}(e^{-i\tau_f\hat{H}_f}e^{-i\tau_i\hat{H}_i})$ is the Franck−Condon factor at temperature T with Z_i the vibrational partition function for the initial electronic state and $H_{i(f)}$ is the vibrational Hamiltonian for the initial or final electronic state.

Based on FGR and the second-order perturbation theory, the general nonradiative decay rate constant can be written as

$$k_{f\leftarrow i} \equiv \frac{2\pi}{\hbar}\sum_{\upsilon,\mu} P_{i\nu} \left| H'_{fu,i\nu} + \sum_{n,\mu} \frac{H'_{fu,n\mu}H'_{n\mu,i\nu}}{E_{i\nu} - E_{n\mu}} \right|^2 \delta(E_{i\nu} - E_{fu}) \tag{7}$$

where H' corresponds to the interaction between two different Born−Oppenheimer states, including two contributions as follows:

$$\hat{H}'\Psi_{i\nu} = \hat{H}^{BO}\Phi_i(\mathbf{r};\mathbf{Q})\Theta_\nu(\mathbf{Q}) + \hat{H}^{SO}\Phi_i(\mathbf{r};\mathbf{Q})\Theta_\nu(\mathbf{Q}) \tag{8}$$

where $\hat{H}^{BO}$ is the nonadiabatic coupling, and $\hat{H}^{SO}$ is the spin−orbit coupling.

The nonradiative rate constant between the two electronic states within the same spin manifold can be expressed according to the first-order perturbation theory as

$$k_{nr} = \frac{1}{\hbar^2}\sum_{kl} R_{kl}\int_{-\infty}^{+\infty} dt\, e^{i\omega_{if}t}\rho_{fi,kl}^{ic}(t, T) \tag{9}$$

where $R_{kl} = \langle\Phi_f|\hat{P}_{fk}|\Phi_i\rangle\langle\Phi_i|\hat{P}_{fl}|\Phi_f\rangle$ is the nonadiabatic electronic coupling matrix element between electronic states Φ_f and Φ_i and $P_{l(k)}$ is the nuclear momentum operator for the $l(k)$-th vibrational normal mode and $\rho_{fi,kl}^{ic}(t, T) = Z_i^{-1}\mathrm{Tr}[\hat{P}_{fk}e^{-i\tau_f\hat{H}_f}\hat{P}_{fl}e^{-i\tau_i\hat{H}_i}]$.

The (reverse) intersystem crossing rate constants from initial singlet/triplet to final triplet/singlet states can be rewritten as

$$k_{ISC/rISC} = \frac{1}{\hbar^2}|H_{fi}^{SO}|^2\int_{-\infty}^{+\infty} dt\, e^{i\omega_{if}t}\rho_{fi}^{ISC/rISC}(t, T) \tag{10}$$

where $\rho_{fi}^{ISC/rISC}(t,T) = Z_i^{-1}Tr(e^{-i\tau_f\hat{H}_f}e^{-i\tau_i\hat{H}_i})$ is the Franck−Condon factor between singlet and triplet states. Our previous work[27,44,45] contains the comprehensive derivation and solution of equations.

All rate constant calculations are performed via the TVCF method in MOMAP 2020B,[46] which has been successfully used to forecast various optoelectrical properties of organic molecules in a wide range of applications.[26−28] We used a Lorentzian-type widening (fwhm = 25 cm^{-1}) in the time domain during the evaluation of the internal conversion rate constant to ensure TVCF convergence. For the conventional TADF molecules, the Herzberg−Teller effect is taken into consideration, because of their high symmetry for the radiative rate constant calculations.[47]

■ ASSOCIATED CONTENT

Supporting Information

The Supporting Information is available free of charge at https://pubs.acs.org/doi/10.1021/acsmaterialslett.1c00794.

Computational details about calculations of PLQY and lifetime, benchmarked data of emission energies and energy gap between lowest singlet and triplet states, optimal tuning parameters of ωb97xd functional, theoretical simulated absorption and emission spectrum, oscillator strengths, theoretical predicted PLQY with experimental results, SOC and adiabatic energy gaps, values of S1 emission cross section and various absorption cross sections at 0−0 or 0−1 emission peak of molecules of group I, S1−S0 reorganization energy projections onto the internal coordinates for p-Cz-BNCz and m-Cz-BNCz (PDF)

■ AUTHOR INFORMATION

Corresponding Authors

Qi Ou − *MOE Key Laboratory of Organic OptoElectronics and Molecular Engineering, Department of Chemistry, Tsinghua University, Beijing 100084, People's Republic of China; AI for Science Institute, Beijing 100080, China;* orcid.org/0000-0002-6400-7522; Email: qiou@mail.tsinghua.edu.cn

Zhigang Shuai − *MOE Key Laboratory of Organic OptoElectronics and Molecular Engineering, Department of Chemistry, Tsinghua University, Beijing 100084, People's Republic of China;* orcid.org/0000-0003-3867-2331; Email: zgshuai@tsinghua.edu.cn

https://doi.org/10.1021/acsmaterialslett.1c00794
ACS Materials Lett. 2022, 4, 487−496

Author

Shiyun Lin − *MOE Key Laboratory of Organic OptoElectronics and Molecular Engineering, Department of Chemistry, Tsinghua University, Beijing 100084, People's Republic of China;* orcid.org/0000-0002-9394-2149

Complete contact information is available at: https://pubs.acs.org/10.1021/acsmaterialslett.1c00794

Notes

The authors declare no competing financial interest.

■ ACKNOWLEDGMENTS

Z.S. is deeply indebted to Professor Daoben Zhu, a pioneering figure in the research field of organic solids, for his longtime encouragements and collaborations. On the occasion of his 80th birthday, we would like to express our sincerest wishes to Prof. Zhu for longevity, healthy and pleasant life. This work is supported by the National Natural Science Foundation of China Grant Nos. 21788102 and 22003030, as well as by the Ministry of Science and Technology of China through the National Key R&D Plan (Grant No. 2017YFA0204501). Q.O. is also funded by China Postdoctoral Science Foundation (Grant No. 2020M670280), as well as the Shuimu Tsinghua Scholar Program. The authors thank Profs. Yongsheng Zhao, Hongbing Fu, and Huanli Dong for inspiring conversations.

■ REFERENCES

(1) Fichou, D.; Delysse, S.; Nunzi, J.-M. First evidence of stimulated emission from a monolithic organic single crystal. *α-Octithiophene* **1997**, *9*, 1178−1181.

(2) Samuel, I. D. W.; Turnbull, G. A. Organic Semiconductor Lasers. *Chem. Rev.* **2007**, *107*, 1272−1295.

(3) Kuehne, A. J. C.; Gather, M. C. Organic Lasers: Recent Developments on Materials, Device Geometries, and Fabrication Techniques. *Chem. Rev.* **2016**, *116*, 12823−12864.

(4) Jiang, Y.; Liu, Y.-Y.; Liu, X.; Lin, H.; Gao, K.; Lai, W.-Y.; Huang, W. Organic solid-state lasers: a materials view and future development. *Chem. Soc. Rev.* **2020**, *49*, 5885−5944.

(5) Li, Y.; Li, S.; He, C.; Zhu, C.; Li, Q.; Li, X.; Liu, K.; Zeng, X. Selective laser-induced preparation of metal-semiconductor nanocomposites and application for enhanced photocatalytic performance in the degradation of organic pollutants. *J. Alloys Compd.* **2021**, *867*, 159062.

(6) Baldo, M. A.; O'Brien, D. F.; Thompson, M. E.; Forrest, S. R. Excitonic singlet-triplet ratio in a semiconducting organic thin film. *Phys. Rev. B* **1999**, *60*, 14422−14428.

(7) Giebink, N. C.; Forrest, S. R. Temporal response of optically pumped organic semiconductor lasers and its implication for reaching threshold under electrical excitation. *Phys. Rev. B* **2009**, *79*, 073302.

(8) Lehnhardt, M.; Riedl, T.; Weimann, T.; Kowalsky, W. Impact of triplet absorption and triplet-singlet annihilation on the dynamics of optically pumped organic solid-state lasers. *Phys. Rev. B* **2010**, *81*, 165206.

(9) Uoyama, H.; Goushi, K.; Shizu, K.; Nomura, H.; Adachi, C. Highly efficient organic light-emitting diodes from delayed fluorescence. *Nature* **2012**, *492*, 234−238.

(10) Zhang, Q.; Tao, W.; Huang, J.; Xia, R.; Cabanillas-Gonzalez, J. Toward Electrically Pumped Organic Lasers: A Review and Outlook on Material Developments and Resonator Architectures. *Adva. Photonics Res.* **2021**, *2*, 2000155.

(11) Lee, J.; Shizu, K.; Tanaka, H.; Nakanotani, H.; Yasuda, T.; Kaji, H.; Adachi, C. Controlled emission colors and singlet−triplet energy gaps of dihydrophenazine-based thermally activated delayed fluorescence emitters. *J. Mater.s Chem. C* **2015**, *3*, 2175−2181.

(12) Dias, F. B.; Penfold, T. J.; Monkman, A. P. Photophysics of thermally activated delayed fluorescence molecules. *Methods and Applications in Fluorescence* **2017**, *5*, 012001.

(13) Montanaro, S.; Gillett, A. J.; Feldmann, S.; Evans, E. W.; Plasser, F.; Friend, R. H.; Wright, I. A. Red-shifted delayed fluorescence at the expense of photoluminescence quantum efficiency − an intramolecular charge-transfer molecule based on a benzodithiophene-4,8-dione acceptor. *Phys. Chem. Chem. Phys.* **2019**, *21*, 10580−10586.

(14) Yang, T.; Cheng, Z.; Li, Z.; Liang, J.; Xu, Y.; Li, C.; Wang, Y. Improving the Efficiency of Red Thermally Activated Delayed Fluorescence Organic Light-Emitting Diode by Rational Isomer Engineering. *Adv. Funct. Mater.* **2020**, *30*, 2002681.

(15) Chen, X.-K.; Kim, D.; Brédas, J.-L. Thermally Activated Delayed Fluorescence (TADF) Path toward Efficient Electroluminescence in Purely Organic Materials: Molecular Level Insight. *Acc. Chem. Res.* **2018**, *51*, 2215−2224.

(16) Kim, D.-H.; D'Aléo, A.; Chen, X.-K.; Sandanayaka, A. D. S.; Yao, D.; Zhao, L.; Komino, T.; Zaborova, E.; Canard, G.; Tsuchiya, Y.; Choi, E.; Wu, J. W.; Fages, F.; Brédas, J.-L.; Ribierre, J.-C.; Adachi, C. High-efficiency electroluminescence and amplified spontaneous emission from a thermally activated delayed fluorescent near-infrared emitter. *Nat. Photonics* **2018**, *12*, 98−104.

(17) Huang, H.; Yu, Z.; Zhou, D.; Li, S.; Fu, L.; Wu, Y.; Gu, C.; Liao, Q.; Fu, H. Wavelength-Turnable Organic Microring Laser Arrays from Thermally Activated Delayed Fluorescent Emitters. *ACS Photonics* **2019**, *6*, 3208−3214.

(18) Ye, H.; Kim, D. H.; Chen, X. K.; Sandanayaka, A. S. D.; Kim, J. U.; Zaborova, E.; Canard, G.; Tsuchiya, Y.; Choi, E. Y.; Wu, J. W.; Fages, F.; Bredas, J. L.; D'Aleo, A.; Ribierre, J. C.; Adachi, C. Near-Infrared Electroluminescence and Low Threshold Amplified Spontaneous Emission above 800 nm from a Thermally Activated Delayed Fluorescent Emitter. *Chem. Mater.* **2018**, *30*, 6702−6710.

(19) Zhou, Z.; Qiao, C.; Wang, K.; Wang, L.; Liang, J.; Peng, Q.; Wei, Z.; Dong, H.; Zhang, C.; Shuai, Z.; Yan, Y.; Zhao, Y. S. Experimentally Observed Reverse Intersystem Crossing-Boosted Lasing. *Angew. Chem., Int. Ed.* **2020**, *59*, 21677−21682.

(20) Khan, A.; Tang, X.; Zhong, C.; Wang, Q.; Yang, S.-Y.; Kong, F.-C.; Yuan, S.; Sandanayaka, A. S. D.; Adachi, C.; Jiang, Z.-Q.; Liao, L.-S. Intramolecular-Locked High Efficiency Ultrapure Violet-Blue (CIE-y < 0.046) Thermally Activated Delayed Fluorescence Emitters Exhibiting Amplified Spontaneous Emission. *Adv. Funct. Mater.* **2021**, *31*, 2009488.

(21) Li, Y.; Wang, K.; Liao, Q.; Fu, L.; Gu, C.; Yu, Z.; Fu, H. Tunable Triplet-Mediated Multicolor Lasing from Nondoped Organic TADF Microcrystals. *Nano Lett.* **2021**, *21*, 3287−3294.

(22) Hatakeyama, T.; Shiren, K.; Nakajima, K.; Nomura, S.; Nakatsuka, S.; Kinoshita, K.; Ni, J.; Ono, Y.; Ikuta, T. Ultrapure Blue Thermally Activated Delayed Fluorescence Molecules: Efficient HOMO−LUMO Separation by the Multiple Resonance Effect. *Adv. Mater.* **2016**, *28*, 2777−2781.

(23) Madayanad Suresh, S.; Hall, D.; Beljonne, D.; Olivier, Y.; Zysman-Colman, E. Multiresonant Thermally Activated Delayed Fluorescence Emitters Based on Heteroatom-Doped Nanographenes: Recent Advances and Prospects for Organic Light-Emitting Diodes. *Adv. Funct. Mater.* **2020**, *30*, 1908677.

(24) Nakanotani, H.; Furukawa, T.; Hosokai, T.; Hatakeyama, T.; Adachi, C. Light Amplification in Molecules Exhibiting Thermally Activated Delayed Fluorescence. *Adv. Opt. Mater.* **2017**, *5*, 1700051.

(25) Ou, Q.; Peng, Q.; Shuai, Z. Computational screen-out strategy for electrically pumped organic laser materials. *Nat. Commun.* **2020**, *11*, 4485.

(26) Shuai, Z.; Peng, Q. Organic light-emitting diodes: theoretical understanding of highly efficient materials and development of computational methodology. *Nat. Sci. Rev.* **2017**, *4*, 224−239.

(27) Shuai, Z. Thermal Vibration Correlation Function Formalism for Molecular Excited State Decay Rates. *Chin. J. Chem.* **2020**, *38*, 1223−1232.

(28) Shuai, Z.; Peng, Q. Excited states structure and processes: Understanding organic light-emitting diodes at the molecular level. *Phys. Rep.* **2014**, *537*, 123−156.
(29) Yang, Z.; Mao, Z.; Xie, Z.; Zhang, Y.; Liu, S.; Zhao, J.; Xu, J.; Chi, Z.; Aldred, M. P. Recent advances in organic thermally activated delayed fluorescence materials. *Chem. Soc. Rev.* **2017**, *46*, 915−1016.
(30) Pershin, A.; Hall, D.; Lemaur, V.; Sancho-Garcia, J.-C.; Muccioli, L.; Zysman-Colman, E.; Beljonne, D.; Olivier, Y. Highly emissive excitons with reduced exchange energy in thermally activated delayed fluorescent molecules. *Nat. Commun.* **2019**, *10*, 597.
(31) Kunze, L.; Hansen, A.; Grimme, S.; Mewes, J.-M. PCM-ROKS for the Description of Charge-Transfer States in Solution: Singlet−Triplet Gaps with Chemical Accuracy from Open-Shell Kohn−Sham Reaction-Field Calculations. *J. Phys. Chem. Lett.* **2021**, *12*, 8470−8480.
(32) Kimber, P.; Goddard, P.; Wright, I. A.; Plasser, F. The role of excited-state character, structural relaxation, and symmetry breaking in enabling delayed fluorescence activity in push−pull chromophores. *Phys. Chem. Chem. Phys.* **2021**, *23*, 26135−26150.
(33) Deshpande, A. V.; Beidoun, A.; Penzkofer, A.; Wagenblast, G. Absorption and emission spectroscopic investigation of cyanovinyl-diethylaniline dye vapors. *Chem. Phys.* **1990**, *142*, 123−131.
(34) Yin, P.-A.; Wan, Q.; Niu, Y.; Peng, Q.; Wang, Z.; Li, Y.; Qin, A.; Shuai, Z.; Tang, B. Z. Theoretical and Experimental Investigations on the Aggregation-Enhanced Emission from Dark State: Vibronic Coupling Effect. *Adv. Electron. Mater.* **2020**, *6*, 2000255.
(35) Lv, L.; Yuan, K.; Zhao, T.; Wang, Y. A new mechanistic study of a second generation TADF material based on the path integral approach incorporating Herzberg−Teller and Duschinsky rotation effects. *J. Mater. Chem. C* **2020**, *8*, 10369−10381.
(36) So, H.; Watanabe, H.; Yahiro, M.; Yang, Y.; Oki, Y.; Adachi, C. Highly photostable distributed-feedback polymer waveguide blue laser using spirobifluorene derivatives. *Opt. Mater.* **2011**, *33*, 755−758.
(37) Laporta, P.; Brussard, M. Design criteria for mode size optimization in diode-pumped solid-state lasers. *IEEE J. Quantum Electron.* **1991**, *27*, 2319−2326.
(38) Dreuw, A.; Head-Gordon, M. Single-Reference ab Initio Methods for the Calculation of Excited States of Large Molecules. *Chem. Rev.* **2005**, *105*, 4009−4037.
(39) Kronik, L.; Kümmel, S. Dielectric Screening Meets Optimally Tuned Density Functionals. *Adv. Mater.* **2018**, *30*, 1706560.
(40) Sun, H.; Zhong, C.; Brédas, J.-L. Reliable Prediction with Tuned Range-Separated Functionals of the Singlet−Triplet Gap in Organic Emitters for Thermally Activated Delayed Fluorescence. *J. Chem. Theory Comput.* **2015**, *11*, 3851−3858.
(41) Frisch, M.; Trucks, G.; Schlegel, H.; Scuseria, G.; Robb, M.; Cheeseman, J.; Scalmani, G.; Barone, V.; Petersson, G.; Nakatsuji, H. et al. *Gaussian 16*; Gaussian. Inc., Wallingford, CT, 2016.
(42) Balasubramani, S. G.; Chen, G. P.; Coriani, S.; Diedenhofen, M.; Frank, M. S.; Franzke, Y. J.; Furche, F.; Grotjahn, R.; Harding, M. E.; Hättig, C.et al. TURBOMOLE: Modular program suite for ab initio quantum-chemical and condensed-matter simulations. *J. Chem. Phys.***2020**, *152*, 184107.
(43) Shao, Y.; Gan, Z.; Epifanovsky, E.; Gilbert, A. T.; Wormit, M.; Kussmann, J.; Lange, A. W.; Behn, A.; Deng, J.; Feng, X.; et al. Advances in molecular quantum chemistry contained in the Q-Chem 4 program package. *Mol. Phys.* **2015**, *113*, 184−215.
(44) Peng, Q.; Niu, Y.; Deng, C.; Shuai, Z. Vibration correlation function formalism of radiative and non-radiative rates for complex molecules. *Chem. Phys.* **2010**, *370*, 215−222.
(45) Peng, Q.; Niu, Y.; Shi, Q.; Gao, X.; Shuai, Z. Correlation Function Formalism for Triplet Excited State Decay: Combined Spin−Orbit and Nonadiabatic Couplings. *J. Chem. Theory Comput.* **2013**, *9*, 1132−1143.
(46) Niu, Y.; Li, W.; Peng, Q.; Geng, H.; Yi, Y.; Wang, L.; Nan, G.; Wang, D.; Shuai, Z. MOlecular MAterials Property Prediction Package (MOMAP) 1.0: a software package for predicting the luminescent properties and mobility of organic functional materials. *Mol. Phys.* **2018**, *116*, 1078−1090.
(47) Niu, Y.; Peng, Q.; Deng, C.; Gao, X.; Shuai, Z. Theory of Excited State Decays and Optical Spectra: Application to Polyatomic Molecules. *J. Phys. Chem. A* **2010**, *114*, 7817−7831.

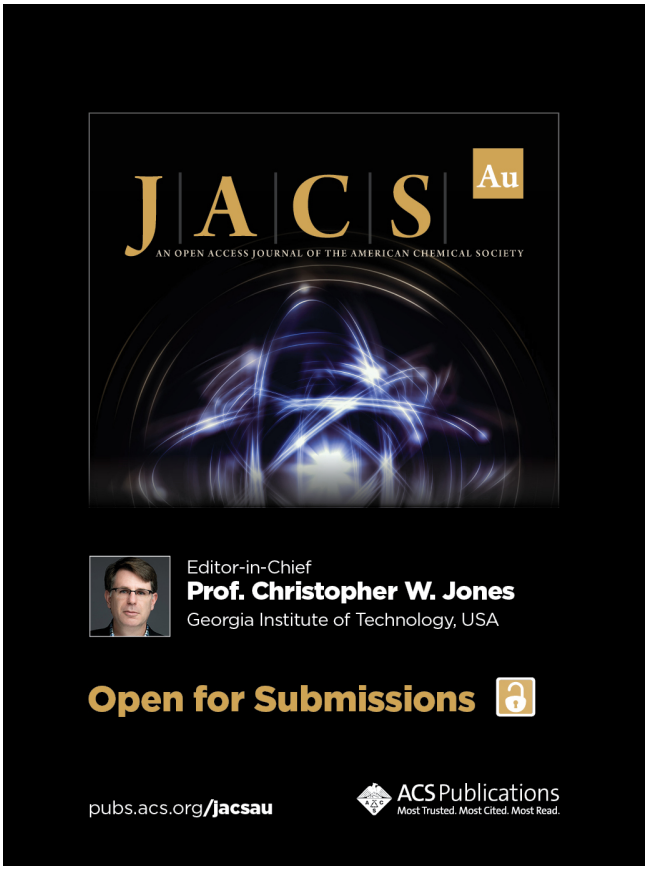

https://doi.org/10.1021/acsmaterialslett.1c00794
ACS Materials Lett. 2022, 4, 487−496